


## Article

# Study on Flow Characteristics of Hydraulic Suction of Seabed Ore Particles

Qiu Xia <sup>1</sup>, Hao Jia <sup>1,\*</sup> , Jiuchun Sun <sup>2</sup>, Xiaoguang Xi <sup>2</sup> and Jingyu Cui <sup>1</sup><sup>1</sup> Key Laboratory of Fluid Transmission Technology of Zhejiang Province, Zhejiang Sci-Tech University, Hangzhou 310018, China<sup>2</sup> Tengda Construction Group Co., Ltd., Taizhou 318000, China

\* Correspondence: jiahao@zstu.edu.cn

**Abstract:** Efficient and environmentally friendly ore collecting operation requires that the ore collecting head can provide just enough suction to start the ore particles in different working conditions. In this work, computational fluid dynamics and discrete element method (CFD-DEM) is used to simulate the hydraulic suction process of ore particles. After analyzing the pressure and velocity characteristics of the flow field, the effects of different suction velocities on the lateral displacement offset, drag coefficient  $C_d$  and Reynolds number  $Re_p$  of particles are studied. It is determined that the lifting force is caused by the different flow velocities of the upper and lower flow fields; particle start-up time and the lateral offset are inversely proportional to suction speed. When  $h/d \geq 2.25$ , the vertical force on particles is no longer affected by  $h/d$ . When  $S/d = 2.5$ ,  $F_Z$  decreases to 0 N; when  $h/d$  increases from 1.5 to 1.75,  $F_Z$  decreases by nearly half. Three empirical equations for  $F_Z$  represented by  $D/d$ ,  $h/d$ , and  $S/d$  are obtained. After integrating the above three equations, the functional relationship of  $F_Z$  with  $D/d$ ,  $h/d$  and  $S/d$  is finally obtained within a certain range. The errors of the equations are within 6%. The particle stress characteristics obtained in this paper can be applied to the establishment of ore collecting performance prediction model and provide data support for the research and development of intelligent ore collecting equipment.

**Keywords:** deep-sea mining; hydraulic suction; particle motion characteristics; solid–liquid two-phase flow; vertical force



**Citation:** Xia, Q.; Jia, H.; Sun, J.; Xi, X.; Cui, J. Study on Flow Characteristics of Hydraulic Suction of Seabed Ore Particles. *Processes* **2023**, *11*, 1376. <https://doi.org/10.3390/pr11051376>

Academic Editors: Lijian Shi, Kan Kan, Fan Yang, Fangping Tang and Wenjie Wang

Received: 4 March 2023

Revised: 26 April 2023

Accepted: 26 April 2023

Published: 2 May 2023



**Copyright:** © 2023 by the authors. Licensee MDPI, Basel, Switzerland. This article is an open access article distributed under the terms and conditions of the Creative Commons Attribution (CC BY) license (<https://creativecommons.org/licenses/by/4.0/>).

## 1. Introduction

With the rapid growth of the global population and economy, a large number of continuous investments in infrastructure construction has increased the consumption of metals. The increasing competition for metal resources in various countries has led to the continuous decline in the grade of land-based mines [1–3]. The survey determined that deep-sea metal nodules are abundant, and deep-sea mineral deposits may make a significant contribution to the future supply of metal raw materials [4,5]. The Clarion–Clipperton Zone (CCZ) in the northeastern Pacific Ocean and the ferromanganese Proto-Crust Zone (PCZ) in the central Pacific Ocean are the most economically valuable areas for metal nodules, in which the total dry tonnage of 15 major metals is conservatively estimated at 211 million tons and 753.3 million tons, respectively [6–8]. Among many marine mineral resources, ferromanganese nodules are the most abundant, with a density of 2100 kg/m<sup>3</sup> and a diameter of 10–120 mm. It is mainly distributed in the seabed at 400–6500 m [4]. In 2000, Morgan et al. [9] determined that the average size of the maximum, median and minimum nodules was 8 cm, 6 cm and 4 cm, respectively. The thickest ferromanganese nodules and the most abundant metal nodules occur at a depth of about 800–2500 m. The distribution of crust and the characteristics of seamounts indicate that mining operations may occur in water depths of about 1500–2500 m [10]. In the 1960s, mining researchers have proposed the concept of deep sea mining (DSM) [11].

Deep-sea mining consists of four components [12]: A mining platform located at the sea surface, the equipment of Ore collecting, Relay station and the hydraulic lifting system (Figure 1). Among them, the seabed collection system is considered as the key technology, because the realization of industrial production requires a high collection rate, at least 140 kg of nodules per second [13,14]. In order to achieve efficient collection, various collection methods such as hydraulic, mechanical and hydraulic–mechanical combination have been developed. The results of OMI [15] sea trial in 1978 showed that the hydraulic collection method had higher collection efficiency than the mechanical collection method. Hydraulic collection [16,17] refers to the process of lifting ore from the seabed to the water surface by using water as the transport medium and moving solid particles upward through the inward flowing water of the pipe. Hydraulic collection is mainly divided into suck-up-based model, Coandă-effect-based model [18] and double-row hydraulic drainage model [19], among which the suction model has the least disturbance to the seabed [20].

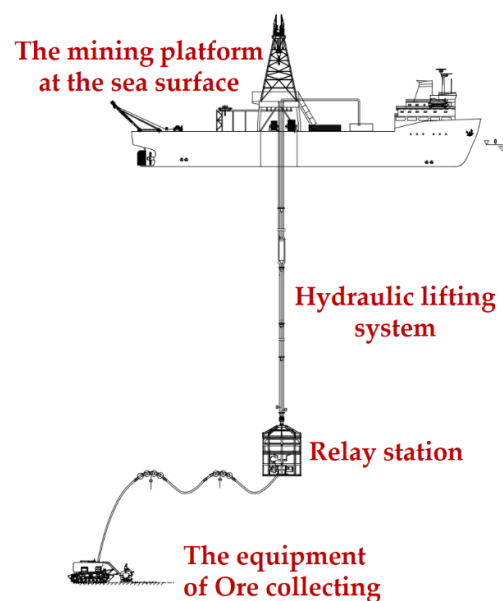


**Figure 1.** The consists of the Deep-sea mining.

Shih et al. [21] determined that the stress characteristics of coarse particles in the flow field are the main basis for the design of seabed collector such as the height of the tubular collector from the seabed  $h$ , the geometric characteristics of ore particles (horizontal long axis length  $a$ , horizontal short axis length  $b$ , vertical axis length  $c$ ), the diameter of the tubular collector  $D$ , the average fluid velocity  $f_v$  in the collector head, the towing velocity  $v_t$  of the collector head, the deviation between the center line of the collector head and the spherical center of particles  $S$ , and the inclination angle  $\theta$  of the collector head. Chen et al. [22] used high-speed imaging and PIV (particle image velocimetry) methods to study the effects of particle diameter  $d$ , ore concentration height  $h$  and particle density  $\rho$  on Froude number  $Fr$  and Reynolds number  $Re$  at particle start-up. It was determined that the wake separation point was located near the top of the particles and the wake vortex facilitated the formation of suction on the particles. In 2017, Zhao et al. [23] combined the experimental and simulation results to produce the relation between the drag coefficient and  $h/d$ . It was concluded that there is little relationship between particle drag coefficient and Reynolds number. In 2018, Zhao et al. [24,25] analyzed the relationship between the ratio of ore collecting head height to particle diameter  $h/d$ , the ratio of ore collecting tube diameter to particle diameter  $D/d$  and the number of vertical suction number  $C_{vs}$ ; an empirical equation with an error of less than 10% was obtained on this basis. The results showed that the wake separation point is near the top of the particle and the wake vortex is conducive to the formation of suction on the particle.

Multi-particle collection has gradually entered the research stage. Sobota et al. [26] conducted an experimental study of the upward flow of nodules and water in a pipe with  $D = 150$  mm and measured the slip velocity of nodules of different diameters at a volume concentration of 10%, concluding that the slip velocity values were of the same order of magnitude as the falling velocity values. Shen et al. [27] studied the influence of particle diameter ratio  $D/d$ , turbulence intensity and particle concentration on particle drag coefficient and particle settling velocity in vertical pipeline hoisting. It was concluded that under certain conditions, the critical Reynolds number of particles advanced, the drag coefficient suddenly dropped to 0.1, the final settling velocity of particles suddenly increased and the minimum hydraulic lifting velocity was introduced. Some scholars have studied the jet collection of particles. Yang and Tang [28] put forward a water jet collector to study the influence of main geometric parameters and condition parameters on the effect of collector. Lee et al. [29] proposed a collector based on Coandă effect of wall-attached jet. After verifying the accuracy of each meta-model, the deep-sea collector based on meta-model was tested.

In the process of particle collection, the movement characteristics and flow field characteristics of particles in the collection tube are also valuable to study [30]. Lim et al. [31] analyzed the flow field characteristics of the acquisition device through Fluent and revealed the velocity distribution characteristics and wake characteristics. Jin et al. [32] used floating experiment to study the minimum lifting velocity, established a formula for the floating velocity and determined that the minimum lifting velocity should be twice the floating velocity of the particles. Xiong et al. [33] used analytical CFD-DEM to simulate the settling and floating motion of spherical particles in vertical pipe and obtained the equations of motion of the particles, revealing the relationship between particle size and floating velocity. Pougatch et al. [34] proposed a numerical model of three-phase flow in upward gas lift pipe and studied the influence of pipe diameter on lifting efficiency. The results showed that this has a significant effect on the gas lift efficiency, and the efficiency increases with the increase in inlet solid particle volume fraction. Relevant scholars have studied the algorithm application of coarse particle numerical simulation. Xiong et al. [33] resolved the CFD-DEM method and compared it with experiments to analyze the feasibility for studying solid–liquid two-phase flow of large particles. Mohammad et al. [35] used a rigorous procedure combining CFD (computational fluid dynamics) and bidirectional FSI (fluid–structure interaction) programs to investigate the effect of sliding on the behavior of a sliding bearing system operating with non-Newtonian lubricants, demonstrating that more realistic results can be obtained using the CFD-FSI approach. Zhu et al. [36] have systematically introduced the CFD-DEM methods, which mainly include the calculation models of particle–particle and particle–fluid interaction.

Scholars mainly use PIV experiment and numerical simulation to study the deep-sea mining particle collection [22]. The CFD-DEM model is mainly used for numerical calculation [32,35]. Previous studies have been conducted on the velocity distribution and particle wake of individual particles collected in vertical pipelines, and research on particle motion characteristics mainly focused on pipelines [31–36]. Quantitative studies of single particle suction mainly focus on the influence of size design on particle stress coefficient, including the relationship between  $h/d$ ,  $D/d$ , particle density  $\rho$ , particle Froude number  $Fr$  and vertical suction number  $C_{vs}$  [23–27]. Moreover, most of the current studies only focus on the influence of single or double factors on the stress of particles. Moreover, no article has studied the three or more sizes of ore collecting equipment together, especially the formula for calculating the force of particles under multiple variables. In addition, the size design of collecting equipment has a great influence on the force of particles [21], and few articles mention the influencing factors such as the dragging velocity  $v_t$  of the collector head, the deviation  $S$  between the center line of the collector head from the center of the particle sphere, and the inclination angle  $\theta$  of the collector head.

In situ deep-sea mining, with long cycle and high cost, is difficult to implement. For laboratory research, most scholars [25,37,38] adopt PIV method to capture images in the

process of particle acquisition. Chen et al. [10,37] performed an experimental testing in a pool with a volume of  $1 \times 1.5 \times 2 \text{ m}^3$ . The pressure sensor was connected at the bottom of the pool, and the motion of particles was captured by PIV equipment. A lot of aspects need to be considered when conducting an experiment. First, deviations and oscillations exist within the pipe during particle collection experiment. Second, due to the different refractive index of particles, water and glass manufacturing tank, there is a certain error in image acquisition. Numerical simulation is cheaper, faster and more accessible than an experiment [39,40]. Therefore, in the study of deep-sea collection of nodules, simulation is usually taken as a pre-study, which not only saves time and resources, but also lays a foundation for the following design of experimental equipment.

In this paper, we simplified the particle collection model and carried out numerical simulation studies on particle collection. This study was conducted by Star-CCM+ 2019.1.1 (14.02.012-R8), a new generation of the CFD software developed by Siemens in Germany. Figure 2 shows the idea behind this paper. First, the flow characteristics of the flow field are analyzed. Next, the effects of suction velocity on particle trajectories, Reynolds number  $Re_p$  and drag coefficient  $C_d$  were summarized. In addition, three main parameters of ore collecting device were selected to research within the appropriate range, which are respectively the diameter—particle size ratio  $D/d$ , collection height—particle size ratio  $h/d$  and particle offset—particle size ratio  $S/d$ . After analyzing the results of 125 examples, the change rules of the vertical force with above three parameters were summarized. On this basis, matlab software and least squares method were used to carry out pairwise fitting of the calculated results. After the three bivariate formulas were obtained, the quadratic fitting of the three formulas was carried out. Ultimately, the calculation formula of the vertical force  $F_z$  on the particle under the action of the three parameters was obtained. According to the empirical formula, the vertical force on the particle can be obtained by adjusting the working condition parameters. The results provide data support for the research and development of intelligent mining equipment.

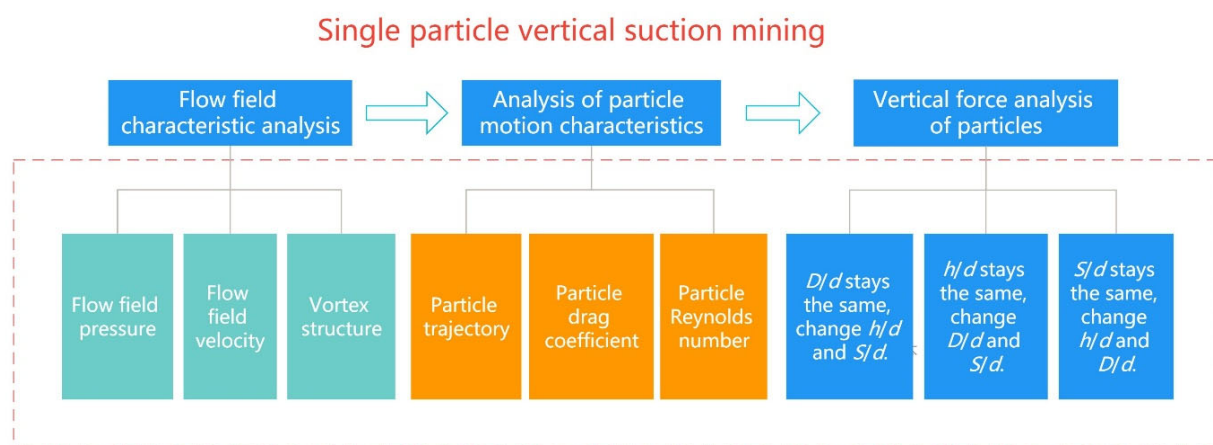


**Figure 2.** Research content of this paper.

## 2. Materials and Methods

### 2.1. Mathematical Model

During particle collection, the interaction between particles and fluid causes particles to lift up along the collection pipeline. In this work, the simulated fluid phase is water, and the mass and momentum conservation equations are solved.

$$\nabla \mathbf{u} = 0, \quad (1)$$

$$\frac{\partial \mathbf{u}}{\partial t} + \mathbf{u} \cdot \nabla \mathbf{u} = -\frac{1}{\rho_f} \nabla p + \nu_f \nabla^2 \mathbf{u} + \mathbf{f}_g + \mathbf{f}_{sf}, \quad (2)$$



where  $f_{sf}$  is the force acting on the fluid by particles,  $\rho_f$  is the density of the fluid,  $f_g$  is the gravity of the fluid, and  $\nu_f$  is the viscosity of the fluid.

The particle collection process is accompanied by intense turbulence. The model Large Eddy Simulation (LES) is used to calculate the turbulent motion of the continuous phase, and the SGS model is used to model the sub-lattice scale stress. In contrast to the RANS equations, the solutions of the LES equations are obtained by spatial filtering rather than averaging process. Each solution variable  $\phi$  is decomposed into a filtered value  $\tilde{\phi}$  and a sub-filtered, or sub-grid value  $\phi'$ :

$$\phi = \tilde{\phi} + \phi', \quad (3)$$

where  $\phi$  represents velocity components, pressure, energy, or species concentration.

The decomposed solution variables are inserted into the Navier–Stokes equations to obtain the equations for the filtered quantities. The filtered equations are rearranged into the same form as the unsteady RANS equations. However, the turbulent stress tensor now represents the subgrid scale stresses. These stresses arise from the interaction between the larger, resolved eddies and the smaller, resolved eddies and are modeled using the Boussinesq approximation as follows:

$$\mathbf{T}_{\text{SGS}} = 2\mu_t \mathbf{S} - \frac{2}{3}(\mu_t \nabla \cdot \tilde{\mathbf{v}}) \mathbf{I}, \quad (4)$$

where  $\mathbf{S}$  is the mean strain rate tensor and  $\tilde{\mathbf{v}}$  is the filtered velocity.

The diameter of the particles is 40 mm, which indicates large-size particles. In the current calculation, the particle translates in the x, y and z direction and rotates around the three axes. By integrating the pressure and shear stress on the surface of particles, the fluid force on particles is obtained, and then the motion equation of 6 DOF (six-degree-of-freedom) body is obtained:

$$m_s \frac{d\mathbf{u}}{dt} = \mathbf{F}_s, \quad (5)$$

$$\mathbf{I}_s \frac{d\boldsymbol{\omega}_s}{dt} + \boldsymbol{\omega}_s \times \mathbf{I}_s \boldsymbol{\omega}_s = \mathbf{M}_s, \quad (6)$$

where  $m_s$  is the mass of the object,  $\mathbf{I}_s$  is the inertia tensor,  $\mathbf{u}$  is the velocity at the center of the object,  $\boldsymbol{\omega}_s$  is the angular velocity of the object, and  $\mathbf{F}_s$  is the resultant force on the rigid body, which can be expressed the calculation equation of the force of the 6-DOF bodies:

$$\mathbf{F}_s = \mathbf{F}_p + \mathbf{F}_\tau + \mathbf{F}_g + \mathbf{f}_f, \quad (7)$$

where  $\mathbf{F}_g$  is the gravity of the particle,  $\mathbf{F}_p$  is fluid pressure,  $\mathbf{F}_\tau$  is fluid shear force and  $\mathbf{f}_f$  is contact coupling force. The component of  $\mathbf{F}_s$  in the Z direction is the vertical force  $F_z$  on the particle.

The Reynolds number of particles is used to reflect the flow state of particles in fluid [19]:

$$Re_p = \frac{\mathbf{u}_{slip} d}{\nu}, \quad (8)$$

where the velocity of particles with respect to the fluid is  $\mathbf{u}_{slip} = \mathbf{u}_f - \mathbf{u}_s$ . The calculation of slip velocity is based on the literature. With  $r$  as the radius, an envelope ball is constructed, and the center of the particle is taken as the center of the ball. Through a series of calculations, a relatively accurate calculation method for the slip velocity of the particle is obtained [21]:

$$\mathbf{u}_{slip} = \frac{1}{4\pi r_s^2} \oint \Omega_{rs} \mathbf{u}_{rel} d\sigma, \quad (9)$$

$$\mathbf{u}_{slip} = u_{slip} \mathbf{e}. \quad (10)$$

The fluid resistance of particles moving in fluid is expressed by dimensionless resistance coefficient  $C_d$ :

$$C_d = \frac{F_z}{\frac{1}{2}\rho_f U_{ref}^2 A_{ref}}, \quad (11)$$

where  $A_{ref}$  is the cross-sectional area of particles.  $U_{ref}$  is the reference velocity, and the pipeline suction velocity  $v$  is taken as the reference velocity. The cross-sectional area of particles is taken as the  $A_{ref}$  in this study.

## 2.2. Physical Modeling and Meshing

The particle collection in vertical pipeline of deep-sea mining is studied, and the following assumptions are proposed:

① Polymetallic nodules are simplified as spherical rigid particles, and the suction process of spherical particles in semi-infinite space is studied.

② Because of the complex mechanical interaction between nodule particles and seabed sediments, the influence of seabed sediments is ignored, and nodule particles are assumed to be located in smooth and rigid bottom.

③ The process of collecting single spherical particles from a clear water vertical pipe is simplified due to the complex interaction between particle and particle or pipe.

The computational domain and associated dimensions are shown in Figure 3. The particle diameter  $d$  is 40 mm, and sufficiently large cylindrical region in the semi-infinite pool is used as the computational domain whose diameter  $D'$  and height  $H$  are  $25d$  and  $7.5d$ , respectively.

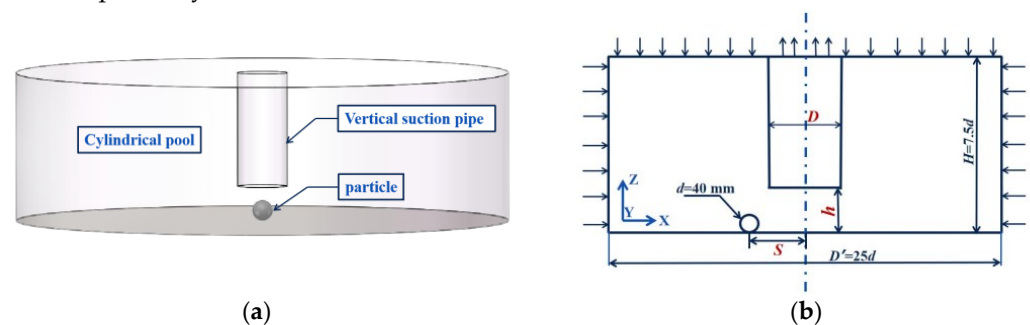


**Figure 3.** Computational domain and size of physical model: (a) Computational domain, (b) Size of physical model.

The meshing of computational domain is shown in Figure 4. The overlapping mesh method is used to calculate the mesh, and a set of overlapping meshes (grey mesh region in Figure 3b) is generated around the particles, which are synchronized with the six-degree-of-freedom motion of the particles. The background region is covered with a set of static meshes (i.e., background mesh, blue mesh in Figure 3b) to cover the entire computational domain. Particle motion equations and fluid control equations are solved in the overlapping meshes to obtain the force and motion characteristics of overlapping meshes, and only the fluid control equations are solved in the background meshes. At the junction of two sets of meshes, the data exchange is performed in a differential way to realize the overall calculation in the control domain. In this work, the diameter of overlapping mesh region is chosen to be twice the diameter of the particle.

In order to consider the accuracy and efficiency of the calculation, the overlapping meshes [41] are encrypted layer by layer as they approach the particle wall. To capture the flow characteristics of the particle trailing region, the overlapping mesh area is adjusted to cover the particle trailing region as much as possible. The background mesh is encrypted layer by layer to maximize the mesh density in the background region closest to the particle motion trajectory (Figure 4b). The scale of the outermost mesh of the overlapping mesh is similar to that of the adjacent background mesh, which ensures reasonable data interaction and improves computational efficiency.

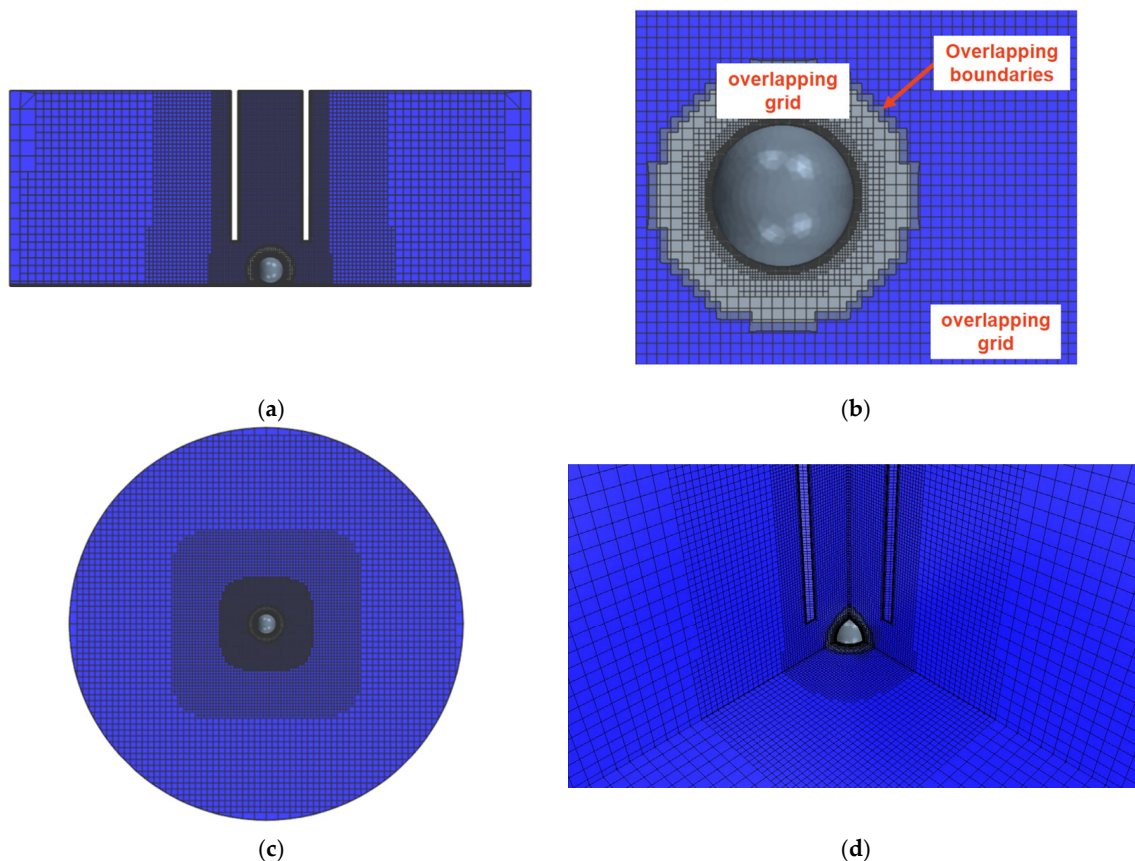


**Figure 4.** Meshing of computational domain: (a) Front view, (b) Locally enlarged grid diagram, (c) Vertical view, (d) xyz profile.

In order not to be impacted by varying mesh sizes, a convergence analysis [41] was conducted to guarantee the quality of the particle collection model. Since the nodule discussed in this work is a coarse particle, the trimmed mesh and the advancing layer mesh are used to generate the meshes which have been shown to be more suitable for the fluid–structure interaction of coarse particles [42]. This work used Star CCM+ software to generate four mesh densities ranging from 3 mm to 2.4 mm at the suction velocity of 1.8 m/s, and compared the calculation of the vertical forces in four models. Table 1 shows grid independence verification. From  $E_1$  to  $E_4$ , the difference in vertical forces between adjacent cases gradually decreases with the increase in grid counts. Among them, the cell quality of  $E_3$  and  $E_4$ , are all larger than 0.3, which meets the calculation requirements. The difference between the vertical force results of  $E_3$  and  $E_4$  is only 0.4%, so the model is considered to have converged at this point. The selection of time step is 0.0003 s, which is consistent with that of Zhao et al. [25]. The mesh size of  $E_3$  is 2.4 mm, which was almost equivalent to results in the previous research [22]. Hence,  $E_3$  was adopted for the final calculation.

**Table 1.** Mesh independence verification.

Case	Number of Meshes	Size of Meshes (mm)	Cell Quality	Time Step (s)	$F$ (N)	Relative Deviation
$E_1$	748,849	3	<0.3	0.0003	0.3469	
$E_2$	1,151,745	2.7	<0.3	0.0003	0.3500	0.89%
$E_3$	1,343,787	2.4	>0.3	0.0003	0.3524	0.69%
$E_4$	1,602,851	2.1	>0.3	0.0003	0.3538	0.4%

### 2.3. Boundary Conditions and Basic Assumptions

As shown in Figure 5, the upper surface and wall of the sink are set as pressure outlets, the collector pipe outlet is set as the velocity outlet boundary condition, and the remaining boundaries are set as walls. The continuous phase medium is liquid water. The particle phase is set to simulate nodules. As shown in Table 2, the simulated particle density is  $2100 \text{ kg/m}^3$ . The gravity direction is downward, opposite to the flow direction.

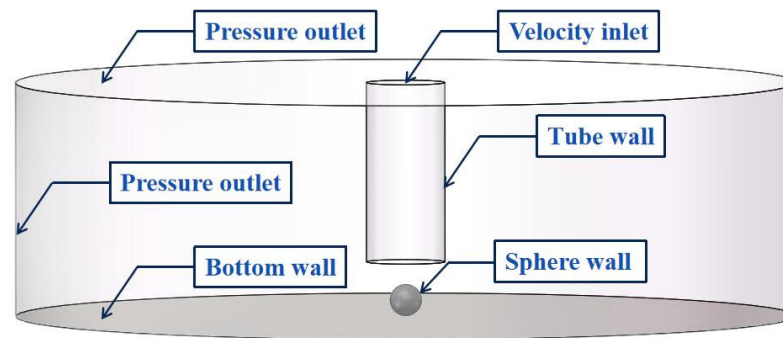


**Figure 5.** Setting of boundary condition.

**Table 2.** Boundary conditions and physical values.

Physical Quantity	Numerical Value	Physical Quantity	Numerical Value
Particle density	$2100 \text{ kg/m}^3$	Particle diameter	40 mm
Fluid density	$1000 \text{ kg/m}^3$	Velocity inlet	2.0–2.8 m/s
Pressure outlet	0.0 Pa	Von Kármán constant	0.42 KPa

The bounded difference is used to solve the pressure, the SIMPLE algorithm is used to solve the coupling of pressure and velocity, and the momentum equation and turbulent kinetic energy equation are discretized by the first-order upwind scheme. The standard residual for the conservation equation of mass and momentum is  $10^{-3}$ .

### 2.4. Algorithm Verification of Model

Figure 6 shows the comparison between the particle vertical force simulated by the algorithm and that measured by Zhao et al. [23] under the conditions of suction velocities  $v = 1.2 \text{ m/s}$ ,  $1.4 \text{ m/s}$ ,  $1.6 \text{ m/s}$ ,  $1.8 \text{ m/s}$  and  $2.0 \text{ m/s}$ , in collection height  $h = 70 \text{ mm}$  and pipe diameter  $D = 100 \text{ mm}$ . Among them, the minimum error is 1.29% and the maximum error is 5.14%. In addition, the average error of the example is 3.73%. Two sets of vertical forces with the smallest errors are presented in Figure 7. We can observe a phenomenon of the vertical force on the particles fluctuating around the mean value, which was also shown in [23]. In this work, the maximum oscillation of vertical force of particles is 0.005 N, which is close to that of Zhao et al. [23]. The simulated values are all consistent with the experimental measurement results. The feasibility and correctness of the algorithm are verified.

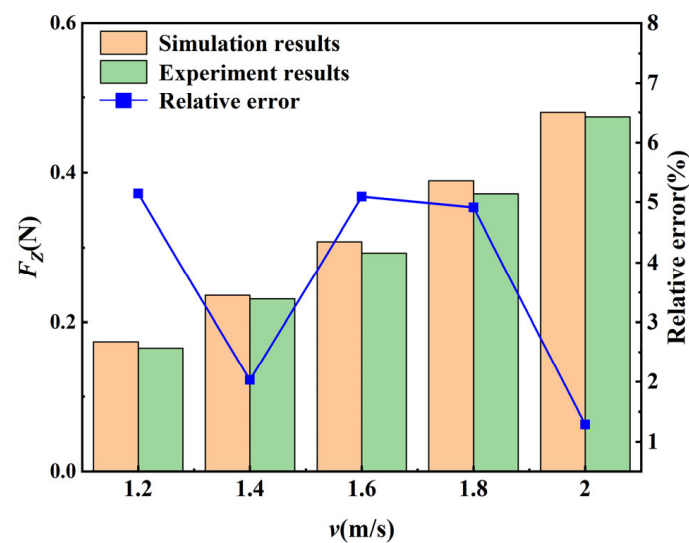


Figure 6. Relative error between simulation and experimental results.

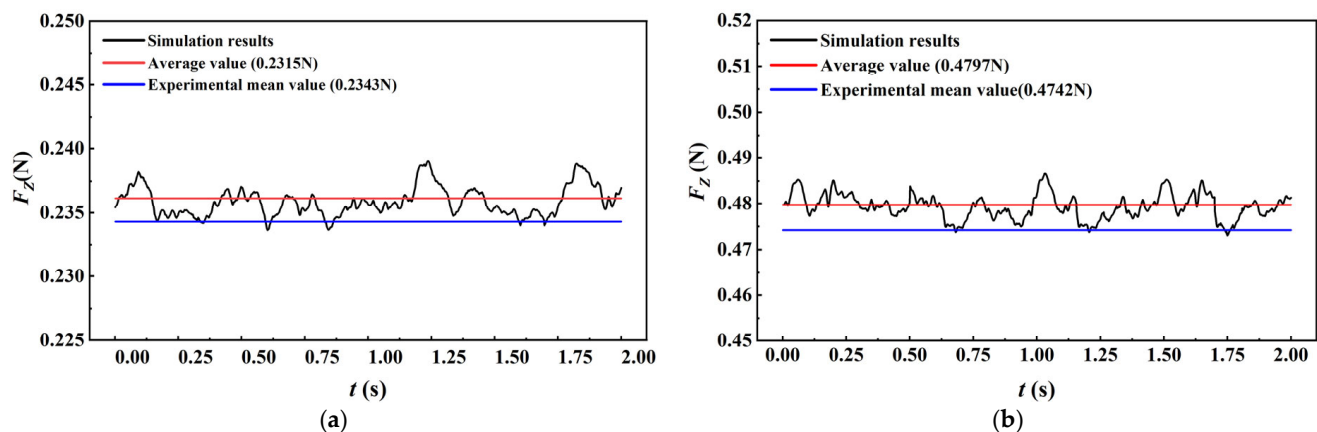


Figure 7. Calculation of vertical force of the particles at  $v = 1.4$  m/s and  $v = 2.0$  m/s: (a)  $v = 1.4$  m/s, (b)  $v = 2.0$  m/s.

### 3. Results and Discussion

This section mainly includes three parts: flow field characteristics, particle motion characteristics and particle force characteristics analysis. By analyzing the flow field characteristics under different suction velocities, the causes of particle initiation by upward lifting force are summarized. The importance of particle initiation conditions is determined by discussing the effects of different suction velocities on particle trajectories, Reynolds number and drag coefficient. The vertical forces on the particles are fixed and calculated for three different conditions, and the empirical equations for the vertical forces on the particles are derived.

#### 3.1. Flow Field Characteristic Analysis

The real condition of the particles being collected in the flowing state is simulated with the suction velocity  $v = 2.0$  m/s. Figure 8 shows the pressure distribution of the flow field when the particle starts up, enters the pipe inlet, move sin the middle of the pipe and approaches the pipe outlet. The fluid pressure acting above the particle is much lower than that acting below the particle, forming the vertical lifting force  $F_z$  of the particle.



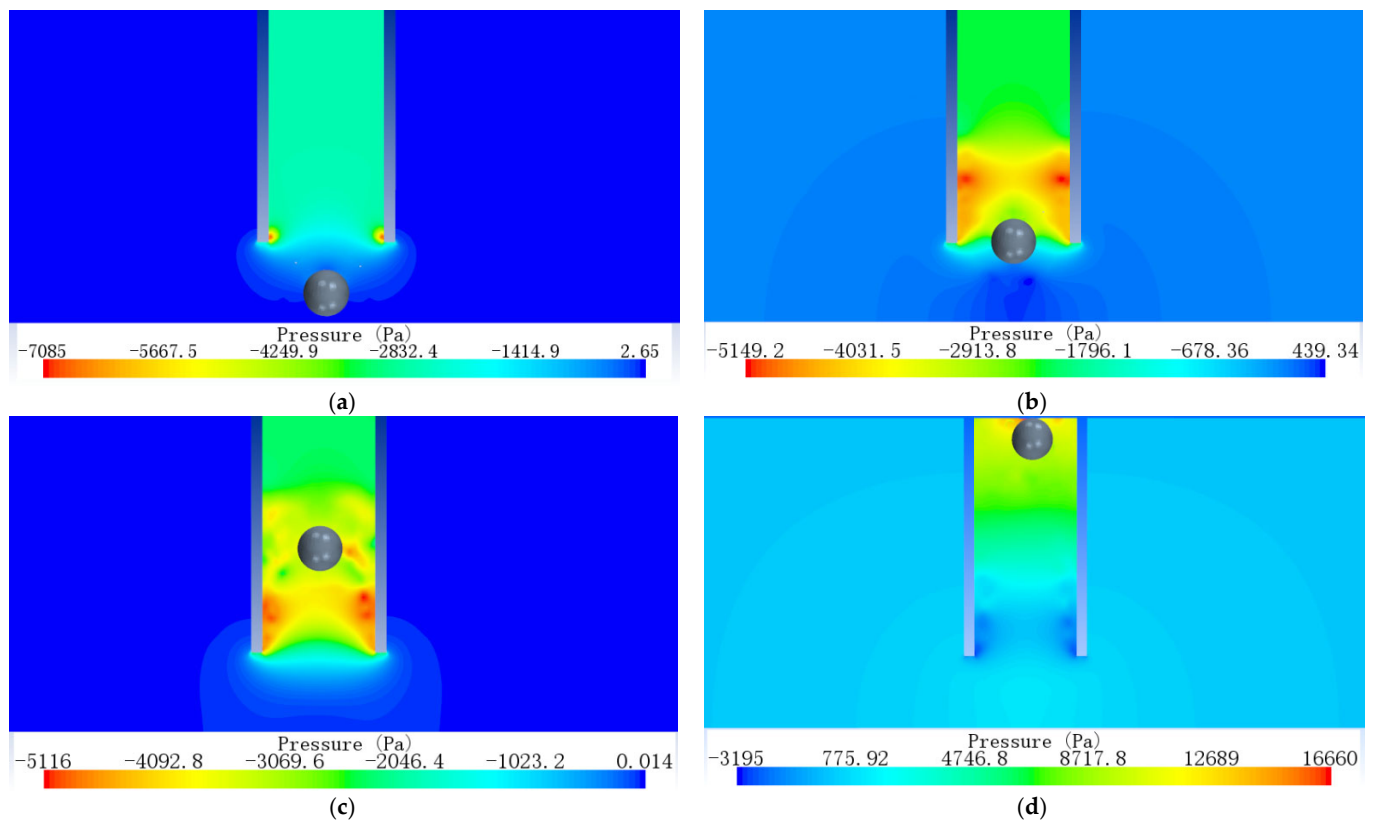


**Figure 8.** Particle pressure distribution at different times: (a)  $t = 0.012$  s, particle start-up, (b)  $t = 0.111$  s, particle entering the pipe port, (c)  $t = 0.159$  s, particle moving in the middle of the pipe, (d)  $t = 0.210$  s, particle approaching the pipe outlet.

Figures 9 and 10 show the velocity field of the flow. In Figure 9a, when the particle starts to be lifted up, the fluid velocity around it is not large, and the flow inside the pipe is laminar. After particle arrives at the entrance of the pipe, the velocity in the pipe increases obviously (Figure 9b). As the particle moves to the center of the pipe, the high-speed area of the flow field in the pipeline evolves around it, and the vortex structure begins to appear at the bottom of the pipe wall (Figure 9c). When the particle approaches the outlet, the turbulence of the flow field around the particle is strengthened (Figure 9d). The particle is surrounded by vortices, resulting in obvious lateral displacement. This phenomenon is consistent with that described by Liu et al. [43], in which the lateral displacement of particles is caused by the effect of wake–wall interaction.

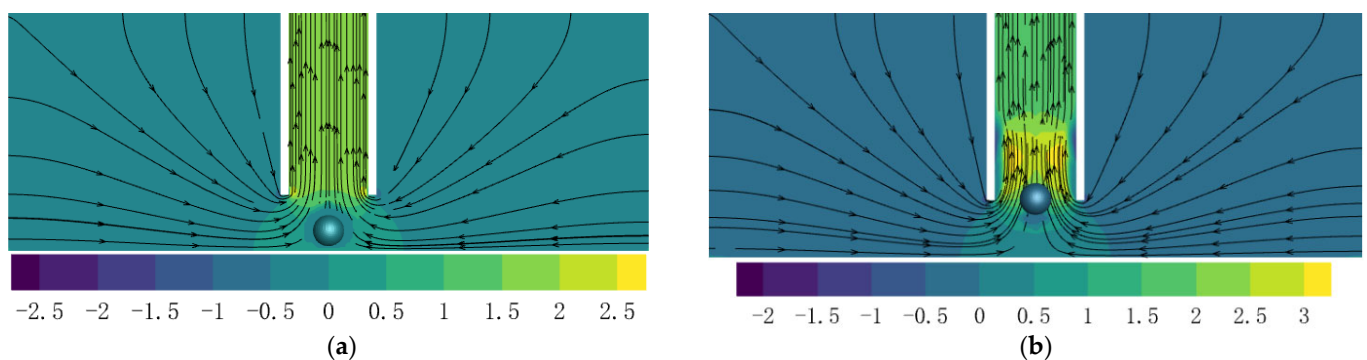


**Figure 9.** Cont.

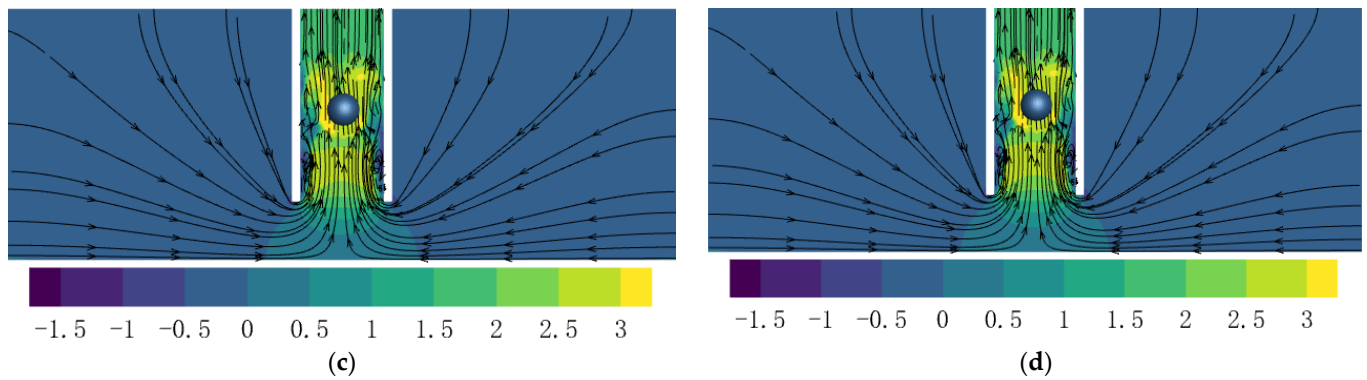


**Figure 9.** Velocity flow diagram at different times: (a)  $t = 0.012$  s, particle start-up, (b)  $t = 0.111$  s, particle entering the pipe port, (c)  $t = 0.159$  s, particle moving in the middle of the pipe, (d)  $t = 0.210$  s, particle approaching the pipe outlet.

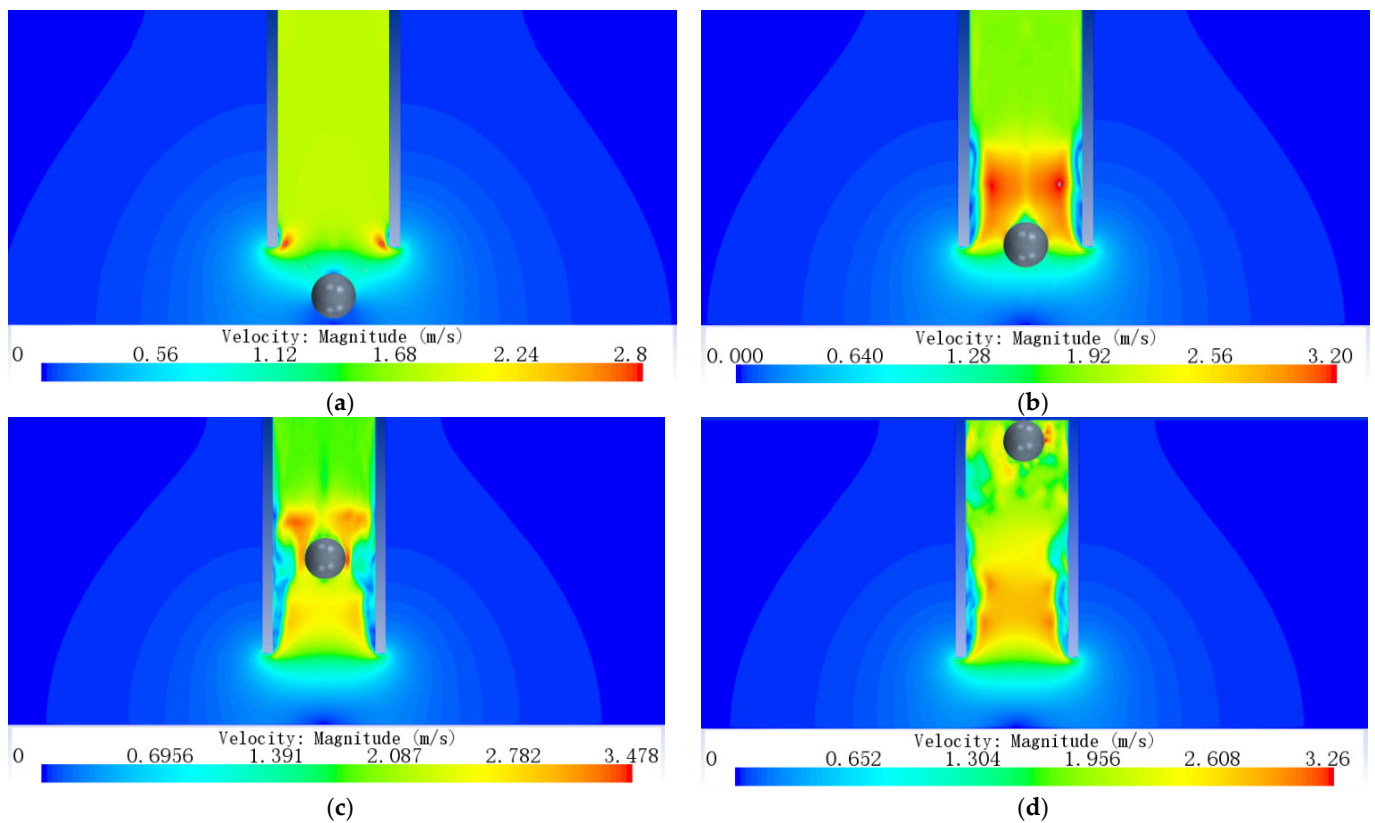


**Figure 10.** Particle velocity nephogram at different times: (a)  $t = 0.012$  s, particle start-up, (b)  $t = 0.111$  s, particle entering the pipe port, (c)  $t = 0.159$  s, particle moving in the middle of the pipe, (d)  $t = 0.210$  s, particle approaching the pipe outlet.

Figure 11 shows the vortex structure around the particles at different times of the suction process. In Figure 11b, we can observe that the wake flow before the particle entering the pipe is obvious, which agrees with the results of Chen's analysis [37], in that the wake is the reason that the vertical force of the particles oscillates around the mean value in Figure 7.



**Figure 11.** Vortex structure around particles: (a)  $t = 0.012$  s, particles start-up, (b)  $t = 0.111$  s, particles enter the pipe port, (c)  $t = 0.159$  s, particles move in the middle of the pipe, (d)  $t = 0.210$  s, particle approaching the pipe outlet.

### 3.2. Analysis of Particle Motion Characteristics

The motion characteristics of particles are important reference factors in deep-sea mining research. The trajectories, Reynolds number and drag coefficient of particles under different initial vertical forces were studied by varying the pipeline suction velocity.

Table 3 shows displacements of particle in three directions, while Figure 12 shows the particle trajectory at a single velocity and different velocities. As can be seen from Figure 12a, the horizontal displacement decreased rapidly after the particle entering the pipe. From Figure 12b and Table 3, it can be seen that the horizontal displacement of the particle increased as the suction velocity decreased. In particular, when the suction velocity  $v$  declined from 2.0 m/s to 1.8 m/s, the horizontal displacement of the particle increased rapidly from 2.4 mm to 8.16 mm. This phenomenon may be caused by the long residence time of particle suspending inside the pipe. The lifting force of the particle decreased with the decrease in suction velocity, while the insufficient lifting force makes the particle suspended in the pipe for a long time. However, when the horizontal displacement is too large, the possibility of particle collision with the pipe wall increases. Collisions and high suction velocities cause unnecessary energy loss. Therefore, in Section 3.3,  $v = 2.0$  m/s is used to study other parameters of the mining device.

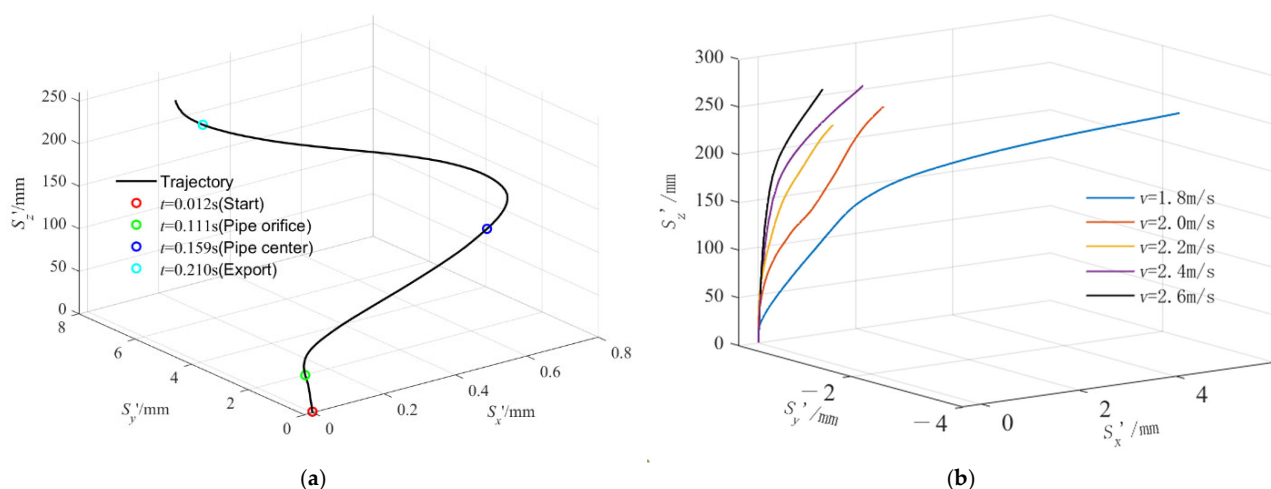


**Figure 12.** Particle trajectory of the suction process: (a) Particle trajectory at  $v = 1.8$  m/s, (b) Particle trajectories at different suction velocities.

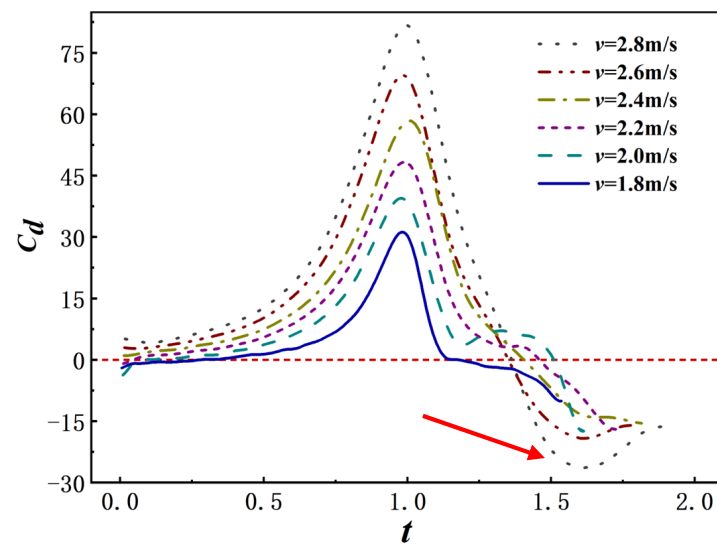
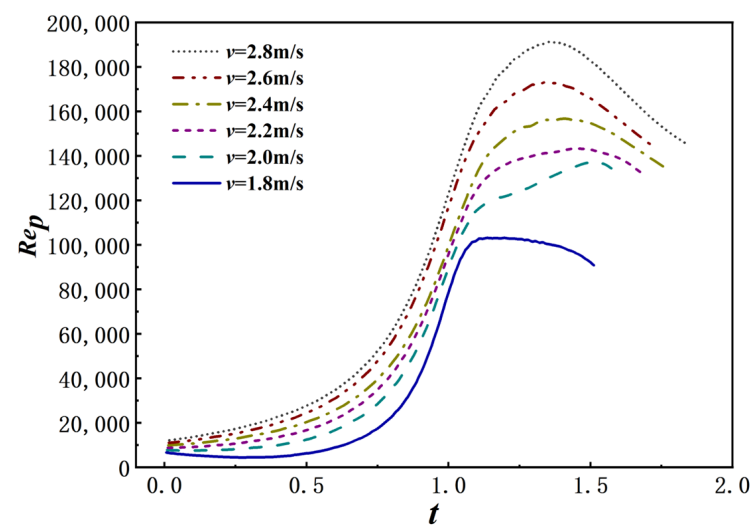
**Table 3.** Maximum offset of particle displacement and suction time.

	$S_X'/\text{mm}$	$S_Y'/\text{mm}$	$S_Z'/\text{mm}$	$(S_X' + S_Y')/\text{mm}$	$t'/\text{s}$
$v = 1.8 \text{ m/s}$	4.8	3.36	260	8.16	0.262
$v = 2.0 \text{ m/s}$	1.17	1.23	260	2.4	0.188
$v = 2.2 \text{ m/s}$	0.51	1.7	260	2.21	0.161
$v = 2.4 \text{ m/s}$	1.88	0.25	260	2.13	0.142
$v = 2.6 \text{ m/s}$	1.08	0.21	260	1.29	0.127

Figures 13 and 14, respectively, show the relationship between drag coefficient  $C_d$  and particle Reynolds number  $Re_p$  with time during particle collection at different suction velocities. Dimensionless time can be expressed as

$$t = \frac{t'}{t_0}, \quad (12)$$

where  $t'$  is the actual movement time of particles, and  $t_0$  is the time when particles move to the pipe port.

**Figure 13.** Variation of particle resistance coefficient  $C_d$  with time  $t$ .**Figure 14.** Variation of particle Reynolds number  $Re_p$  with time  $t$ .

It can be observed that the drag coefficient  $C_d$  and Reynolds number  $Re_p$  reach peak values when the particles are close to the pipe inlet during the collection process, and the values of  $C_d$  and  $Re_p$  decrease after entering the pipe. With the increase in suction velocity, the maximum values of  $C_d$  and  $Re_p$  increase gradually, which causes the fluctuation of particles in the collection process to increase, and then increases the possibility of collision between particles and the inner wall of the pipeline, and increases unnecessary energy loss. In addition, in the whole collection process, the displacement between the particle start-up and the collection port is only one sixth of the total displacement, as shown in Figure 12a (50 mm/300 mm), and the time consumed by the particle moving to the collection port is about one half of the total time (0.95/1.75). Obviously, the particle start-up process is the most time-consuming stage. After entering the pipeline,  $C_d$  and  $Re_p$  decreased significantly, and the higher the suction velocity, the smaller the minimum values of  $C_d$  and  $Re_p$  (see the red arrow).

### 3.3. Vertical Force Analysis of Particles

The analysis of particle trajectories, particle Reynolds number and drag coefficients revealed that the particles take the longest time during the start-up stage. However, the initial conditions have significant influence on the trajectory of particles, the maximum value of drag coefficient  $C_d$  and Reynolds number  $Re_p$ . In order to obtain the quantitative law between  $F_Z$  and  $D/d$ ,  $h/d$  and  $S/d$ , 75 simulation examples under three conditions ( $v = 2.0$  m/s and  $d = 40$  mm) are analyzed (as shown in Table 4). According to the variable research results [24,25], the effective ranges of most of the variables studied are  $-2.5 \leq S/d \leq 2.5$ ,  $1.4 \leq h/d \leq 2.4$ , and  $1.875 \leq D/d \leq 4.0$ . The research scope is  $0 \leq S/d \leq 2.5$ ,  $1.5 \leq h/d \leq 2.5$ , and  $2.0 \leq D/d \leq 4.0$ . Particle Reynolds number  $Re_p$  range is  $3524.11 \leq Re_p \leq 2,593,804.9$ .

**Table 4.** Calculated working conditions.

	$h/d$	$D/d$	$S/d$
Working condition of the one	1.5	2, 2.5, 3, 3.5, 4	0
	1.75	2, 2.5, 3, 3.5, 4	0
	2	2, 2.5, 3, 3.5, 4	0
	2.25	2, 2.5, 3, 3.5, 4	0
	2.5	2, 2.5, 3, 3.5, 4	0
Working condition of the two	1.5	2.5	0, 0.625, 1.25, 1.875, 2.5
	1.75	2.5	0, 0.625, 1.25, 1.875, 2.5
	2	2.5	0, 0.625, 1.25, 1.875, 2.5
	2.25	2.5	0, 0.625, 1.25, 1.875, 2.5
	2.5	2.5	0, 0.625, 1.25, 1.875, 2.5
Working condition of the three	1.75	2	0, 0.625, 1.25, 1.875, 2.5
	1.75	2.5	0, 0.625, 1.25, 1.875, 2.5
	1.75	3	0, 0.625, 1.25, 1.875, 2.5
	1.75	3.5	0, 0.625, 1.25, 1.875, 2.5
	1.75	4	0, 0.625, 1.25, 1.875, 2.5

After the computational results are obtained, the empirical equations of  $F_Z$  expressed by  $D/d$  and  $h/d$ ,  $h/d$  and  $S/d$ ,  $D/d$  and  $S/d$  are determined. Finally, the empirical equations of  $F_Z$  expressed by  $D/d$ ,  $h/d$  and  $S/d$  are obtained by fitting the model with the least square method by one-to-one correspondence between the data of the three variables and  $F_Z$  value.

Figure 15 shows the relationship between the vertical force  $F_Z$  on the particles and the ratio of pipe diameter to particle diameter  $D/d$  and the ratio of height from ore head to seabed to particle diameter  $h/d$  when  $S/d = 0$ . The higher the particle collection height and the smaller the pipe diameter, the smaller the turbulence degree of particles around the fluid, and the smaller the force of the fluid on the particles. Therefore,  $F_Z$  is inversely proportional to  $h/d$  and directly proportional to  $D/d$ , and with the increase in  $h/d$ ,  $F_Z$  becomes more and more gentle. When  $h/d \geq 2.25$ , the vertical force on the particle is



no longer affected by  $h/d$ . The variation trend of  $F_Z$  with  $D/d$  and  $h/d$  is very close to the findings of Zhao et al. [24]. The empirical equations of  $F_Z$  expressed in  $D/d$  and  $h/d$  are obtained:

$$F_Z = \frac{p_1 + p_2 * h/d + p_3 * D/d}{2[1 + p_4 * h/d + p_5 * (h/d)^2 + p_6 * D/d]} \rho_{ref} U_{ref} A_{ref}, \quad (13)$$

where  $p_1 = -0.015406749$ ,  $p_2 = -0.019219455$ ,  $p_3 = 0.034382130$ ,  $p_4 = -1.504965261$ ,  $p_5 = 0.565836045$ ,  $p_6 = 0.035174519$ , and the sum of squares of correlation coefficients  $R_2 = 0.999316'$ ,  $2.0 \leq D/d \leq 4.0$ ,  $1.5 \leq h/d \leq 2.5$ .

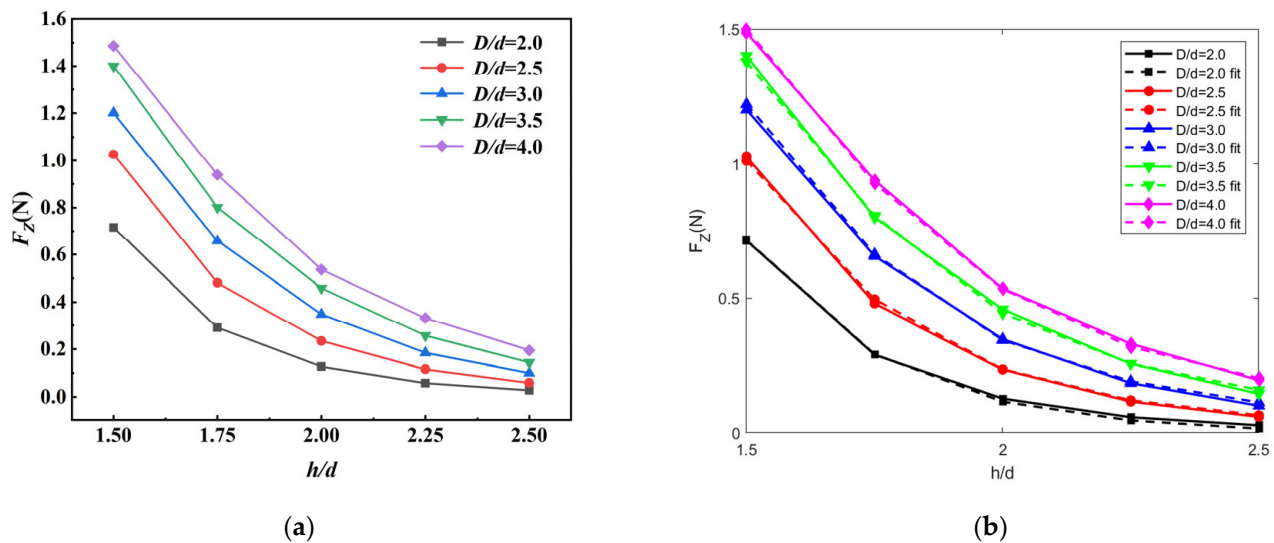


**Figure 15.** The relationship between  $F_Z$  and  $D/d$ ,  $h/d$  when  $S/d = 0$ : (a) Before fitting, (b) After fitting.

Figure 16 shows the relationship between the vertical force  $F_Z$  on the particles and the ratio  $h/d$  of the height of the head from the seabed to the particle diameter and the ratio  $S/d$  of the particle offset to the particle diameter when  $D/d = 2.5$ . It can be seen that  $F_Z$  is inversely proportional to  $h/d$  and  $S/d$ . When  $S/d \geq 1.85$ ,  $F_Z$  decreases to about 0 N. Because the center of the particle is too far away from the center of the pipe, the fluid around the particle almost no longer flows, and the particle is no longer stressed. When  $h/d$  increased from 1.5 to 1.75,  $F_Z$  decreased by almost half (1.0261 N/0.4804 N). Zhao et al. [44] used  $\theta$  to represent the offset angle between the pipe and the bottom end of the ore particle, and discussed the change in vertical force on particle with  $\theta$ . There is a high level of agreement between the study of Zhao and this study. The empirical equation of  $F_Z$  expressed in terms of  $h/d$  and  $S/d$  is obtained:

$$F_Z = \frac{n_1 + n_2 * S/d + n_3 * h/d}{2[1 + n_4 * S/d + n_5 * (S/d)^2 + n_6 * (S/d)^3 + n_7 * h/d + n_8 * (h/d)^2]} \rho_{ref} U_{ref} A_{ref}, \quad (14)$$

where  $n_1 = 4909.333762474$ ,  $n_2 = -715.763350549$ ,  $n_3 = -1539.484080196$ ,  $n_4 = -3095.756930924$ ,  $n_5 = -69.677246409$ ,  $n_6 = 4803.659602331$ ,  $n_7 = -9353.720063242$ ,  $n_8 = 9126.598099038$ ,  $1.5 \leq h/d \leq 2.5$ ,  $0 \leq S/d \leq 2.5$ .

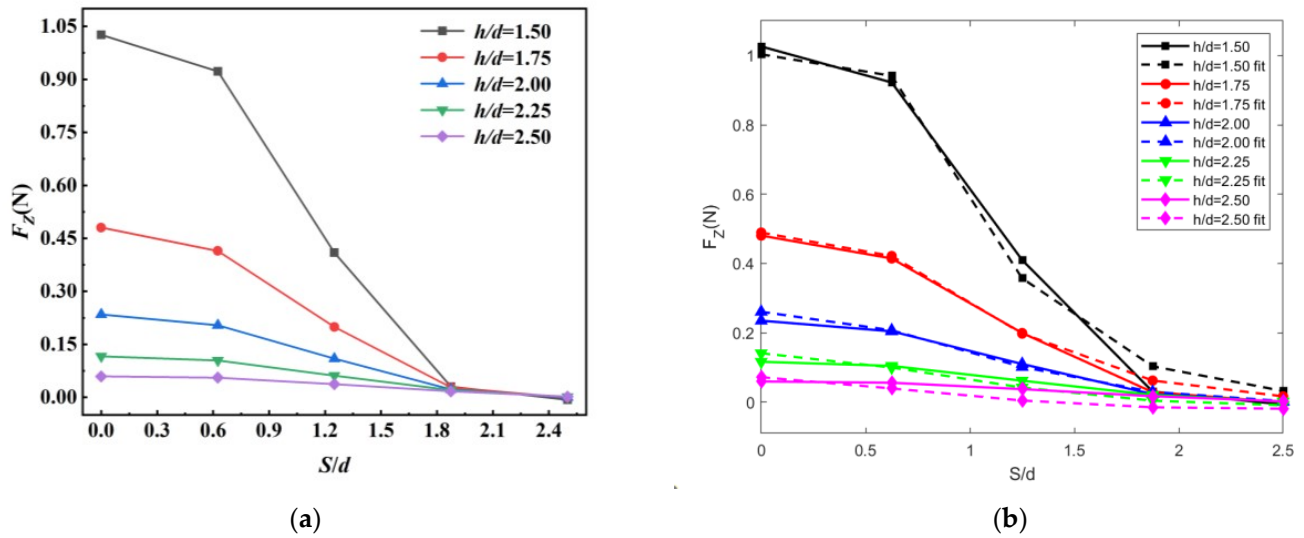


**Figure 16.** The relationship between  $F_Z$  and  $h/d$  and  $S/d$  when  $D/d = 2.5$ : (a) Before fitting, (b) After fitting.

Figure 17 shows the relationship between the vertical force  $F_Z$  on the particles and  $D/d$  and  $S/d$  when  $h/d = 1.75$ . When  $S/d \leq 0.6$ ,  $F_Z$  is almost independent by the size of  $S/d$  and  $F_Z$  decreases steadily with the gradual increase in  $D/d$ . When  $S/d$  increases to 2.5,  $F_Z$  decreases to 0 N. The empirical equation of  $F_Z$  expressed by  $D/d$  and  $S/d$  is obtained:

$$F_Z = \frac{m_1 + m_2 * S/d + m_3 * D/d}{2[1 + m_4 * S/d + m_5 * (S/d)^2 + m_6 * S/d + m_7 * D/d]} \rho_{ref} U_{ref} A_{ref}, \quad (15)$$

where  $m_1 = -0.196683548$ ,  $m_2 = -0.093600961$ ,  $m_3 = 0.169117107$ ,  $m_4 = 0.270094103$ ,  $m_5 = -1.447796059$ ,  $m_6 = 0.979306132$ ,  $m_7 = 0.069992649$ , and the sum of squares of correlation coefficients  $R_2 = 0.991839'$ ,  $2.0 \leq D/d \leq 4.0$  and  $0 \leq S/d \leq 2.5$ .

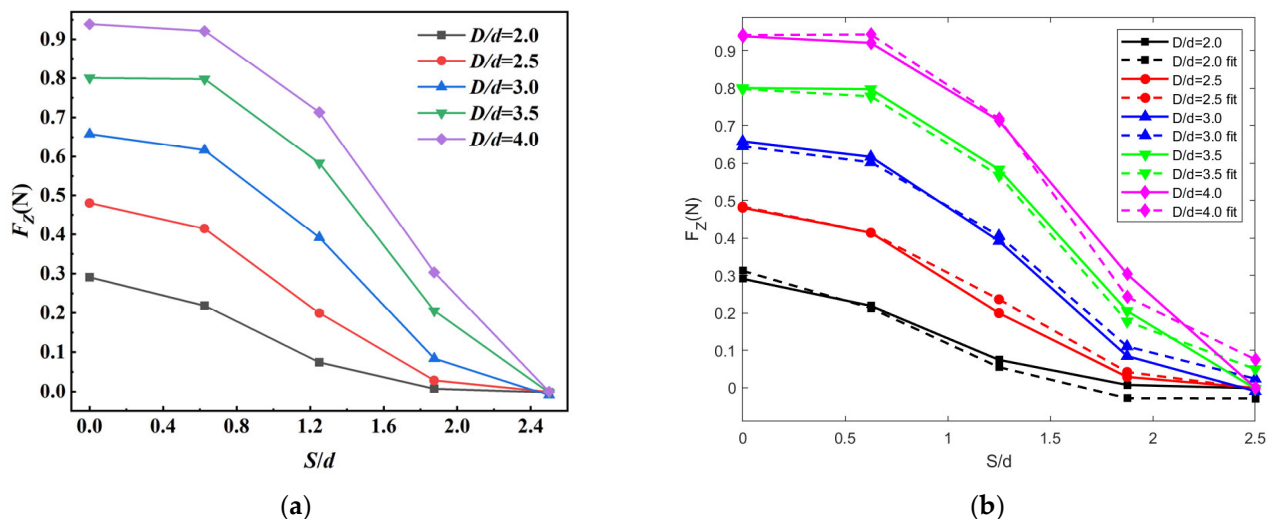


**Figure 17.** The relationship between  $F_Z$  and  $D/d$  and  $S/d$  when  $h/d = 1.75$ : (a) Before fitting, (b) After fitting.

Finally, the empirical equation of  $F_Z$  expressed in  $S/d$ ,  $h/d$  and  $D/d$  is

$$F_Z = \frac{k_1 + k_2 * x_1 + k_3 * (x_1)^2 + k_4 * x_2 + k_5 * x_3 + k_6 * (x_3)^2}{2[1 + k_7 * x_1 + k_8 * (x_1)^2 + k_9 * x_2 + k_{10} * (x_2)^2 + k_{11} * (x_3)^2]} \rho_{ref} U_{ref} A_{ref}, \quad (16)$$

where  $x_1 = S/d$ ,  $x_2 = h/d$ ,  $x_3 = D/d$ ,  $k_1 = 0.010957197$ ,  $k_2 = -0.000972665$ ,  $k_3 = -0.005222932$ ,  $k_4 = -0.010161059$ ,  $k_5 = 0.003012223$ ,  $k_6 = 0.004227619$ ,  $k_7 = -0.067167101$ ,  $k_8 = 0.097555715$ ,  $k_9 = -1.397898770$ ,  $k_{10} = 0.513337409$ ,  $k_{11} = 0.001072299$ , and the sum of squares of correlation coefficients  $R_2 = 0.991047$ ,  $0 \leq S/d \leq 2.5$ ,  $1.5 \leq h/d \leq 2.5$ ,  $2.0 \leq D/d \leq 4.0$ ,  $3524.11 \leq Re_p \leq 2,593,804.9$ .

After obtaining the final fitting Formula (16), four working conditions within the range of variables were randomly selected (as shown in Table 5 and Figure 18). In this paper, the calculation results and simulation results under four working conditions are compared and error analysis is conducted. The results show that all errors are within 6%, the maximum error is 5.50%, and the minimum error is 0.46%. The results show that the empirical formula is accurate and can be used to predict the vertical force of particles.

**Table 5.** The relative error between simulation result and formula calculation results.

Data Groups	$h/d$	$D/d$	$S/d$	$v$ (m/s)	Simulation Results (N)	Formula Calculation Results (N)	Relative Error (%)
1	1.7	2.6	1.2	2	0.29152	0.28948	0.70
2	2.2	2.1	0.7	2.1	0.06850	0.068183	0.46
3	2	2.5	1.9	2.3	0.2723	0.025887	4.93
4	2.2	2.75	1	2.2	0.43049	0.40682	5.50

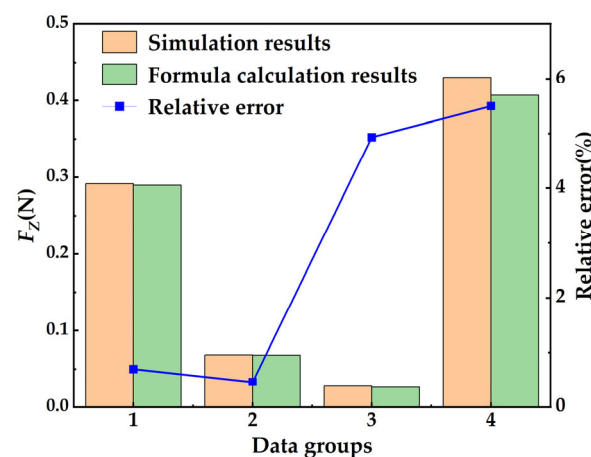


**Figure 18.** The relative error between simulation result and formula calculation result.

In addition, due to different working conditions, it is difficult to make a large number of comparisons between the results of the final example and those of other scholars. Only 10 examples in working conditions 1 are compared with the results of Zhao et al. [23], and the errors are all within 5%. Compared with the particle force coefficient formula proposed by Zhao et al. [23–25] based on univariate ( $h/d$ ) or bivariate ( $h/d$ ,  $D/d$ ), this formula shows the relationship between the vertical force on the particle and three variables ( $h/d$ ,  $D/d$ ,  $S/d$ ). These empirical formulas can predict the vertical force on the particles relatively accurately, and further provide a reference for the research of hydraulic mining mechanism and accurate mining of mineral particles in deep-sea mining. In order to improve the collection rate of harvester operation and reduce the influence of unnecessary disturbance on the seabed, the key parameters such as  $D$ ,  $h$  and  $S$  in the harvester system can be adjusted in real time based on the formula to provide appropriate suction for ore particles.

In this paper, investigation of particle collection on deep-sea mining is simplified into a model of a single particle sucked through a pipe. In fact, to reach a more accurate and convincing conclusion, experiments are needed as auxiliary evidence [45–47]. Study without experimentation is a limitation of this article. In this work, the numerical simulation method is used to analyze the particle collection in some aspects, which can be regarded as preliminary research before performing the experimentation.

#### 4. Conclusions

In this work, the feasibility and correctness of the calculation method were verified using the experimental data of Zhao et al. [23]. Then, the hydraulic suction process of ore particles was simulated, and the flow field characteristics and particle motion characteristics under different suction velocities were analyzed. The vertical force on fixed particles under different  $D/d$ ,  $h/d$  and  $S/d$  conditions were simulated and calculated. In the following research, we will continue to conduct multi-particle collection simulation and build an experimental testing so as to make the research more credible. The following conclusions were drawn:

The lifting force of particles in the suction process is caused by the different flow velocities above and below the particles. In the process of particle collection, the distribution of vortex structure on the particle surface changes from annular at the inlet to around the particle, and the vortex under the particle increases when it reaches the outlet of the pipe.

At different suction velocities, the trajectories of the particles before entering the pipeline are basically the coincident. After the particles enter the pipeline, the lateral offset starts to increase. Moreover, the smaller the suction velocity, the slower the particle start-up and the longer the suction time, which leads to larger final lateral offset of particles. If the suction velocity is too small, it will increase the possibility of collision between particles and pipeline wall. However, if the suction velocity is too high, the energy loss will increase. It proves that it is necessary to select suitable particle start-up conditions.

The particle initiation process is the most time-consuming stage, and it has high research value. The drag coefficient  $C_d$  and Reynolds number  $Re_p$  of the particles reach the peak when they reach the pipe inlet. After entering the pipeline,  $C_d$  and  $Re_p$  decrease significantly. The higher the suction rate, the greater the peak value of  $C_d$  and  $Re_p$ .

The vertical force  $F_Z$  is inversely proportional to  $h/d$  and  $S/d$  and directly proportional to  $D/d$ . When  $h/d \geq 2.25$ , the vertical force on particles is no longer affected by  $h/d$ . When  $S/d = 2.5$ ,  $F_Z$  decreased to 0 N; when  $h/d$  increased from 1.5 to 1.75,  $F_Z$  decreased by nearly half. The empirical equations of  $F_Z$  expressed in terms of  $D/d$  and  $h/d$ ,  $h/d$  and  $S/d$ ,  $D/d$  and  $S/d$  were obtained (13), (14) and (15). Finally, the empirical equations of  $F_Z$  (16) expressed in  $S/d$ ,  $h/d$  and  $D/d$  were obtained. The error of the formula is within 6%.

**Author Contributions:** Conceptualization, Q.X. and H.J.; methodology, Q.X.; software, Q.X.; validation, J.S., X.X. and J.C.; formal analysis, Q.X.; investigation, Q.X.; resources, H.J.; data curation, J.S.; writing—original draft preparation, Q.X.; writing—review and editing, Q.X.; visualization, Q.X.; supervision, J.C.; project administration, H.J.; funding acquisition, H.J. All authors have read and agreed to the published version of the manuscript.

**Funding:** This research was funded by the National Nature Science Foundation of China (52206056, 52071296), Key Research and Development Program of Zhejiang Province (2022C01168).

**Data Availability Statement:** Not applicable.

**Conflicts of Interest:** The authors declare no conflict of interest.

#### References

1. Beyond mining. *Nat. Geosci.* **2011**, *4*, 653. [\[CrossRef\]](#)
2. Hein, J.R.; Mizell, K.; Koschinsky, A.; Conrad, T.A. Deep-ocean mineral deposits as a source of critical metals for high- and green-technology applications: Comparison with land-based resources. *Ore Geol. Rev.* **2013**, *51*, 1–14. [\[CrossRef\]](#)
3. Mudd, G.M. The Environmental sustainability of mining in Australia: Key mega-trends and looming constraints. *Resour. Policy* **2009**, *35*, 98–115. [\[CrossRef\]](#)
4. Lusty, P.A.; Murton, B.J. Deep-Ocean Mineral Deposits: Metal Resources and Windows into Earth Processes. *Elements* **2018**, *14*, 301–306. [\[CrossRef\]](#)
5. Abramowski, T.; Urbanek, M.; Baláž, P. Structural Economic Assessment of Polymetallic Nodules Mining Project with Updates to Present Market Conditions. *Minerals* **2021**, *11*, 311. [\[CrossRef\]](#)
6. Jones, D.O.B.; Simon-Lledó, E.; Amon, D.J.; Bett, B.J.; Caille, C.; Clément, L.; Connelly, D.P.; Dahlgren, T.G.; Durden, J.M.; Drazen, J.C.; et al. Environment, ecology, and potential effectiveness of an area protected from deep-sea mining (Clarion Clipperton Zone, abyssal Pacific). *Prog. Oceanogr.* **2021**, *197*, 102653. [\[CrossRef\]](#)

7. Maciag, Ł.; Harff, J. Application of multivariate geostatistics for local-scale lithological mapping—Case study of pelagic surface sediments from the Clarion-Clipperton Fracture Zone, north-eastern equatorial Pacific (Interoceanmetal claim area). *Comput. Geosci.* **2020**, *139*, 104474. [[CrossRef](#)]
8. Petersen, S.; Krättschell, A.; Augustin, N.; Jamieson, J.; Hein, J.R.; Hannington, M.D. News from the seabed—Geological characteristics and resource potential of deep-sea mineral resources. *Mar. Policy* **2016**, *70*, 175–187. [[CrossRef](#)]
9. Moore, G.W. Handbook of Marine Mineral Deposits. *Eos Trans. Am. Geophys. Union* **2000**, *81*, 411–413. [[CrossRef](#)]
10. Hein, J.R.; Conrad, T.A.; Dunham, R.E. Seamount Characteristics and Mine-Site Model Applied to Exploration- and Mining-Lease-Block Selection for Cobalt-Rich Ferromanganese Crusts. *Mar. Georesources Geotechnol.* **2009**, *27*, 160–176. [[CrossRef](#)]
11. Mero, J.L. section of geological sciences: Mineral resources of the sea. *Trans. N. Y. Acad. Sci.* **1964**, *26*, 525–544. [[CrossRef](#)]
12. Oebius, H.U.; Becker, H.J.; Rolinski, S.; Jankowski, J.A. Parametrization and evaluation of marine environmental impacts produced by deep-sea manganese nodule mining. *Deep. Sea Res. Part II Top. Stud. Oceanogr.* **2001**, *48*, 3453–3467. [[CrossRef](#)]
13. Chung, J.S. Advances in Manganese-Nodule Mining Technology. *Mar. Technol. Soc. J.* **1985**, *19*, 39–44.
14. Herrouin, G.; Lenoble, J.P.; Charles, C.; Mauviel, F.; Bernard, J.; Taine, B. A manganese nodule industrial venture would be profitable: Summary of a 4-year study in France. In Proceedings of the 21st Annual Offshore Technology Conference, OTC 1989, Houston, TX, USA, 1–4 May 1989; pp. 321–332.
15. Zhao, S.N.; Liu, F. Research on deep sea mining technology in Germany. *Met. Mines* **1995**, *6*, 14–17. (In Chinese)
16. Liu, L. Study on the Mechanical Characteristics of Solid-Liquid Two-Phase Flow by Hydraulic Lifting in Deep Sea Mining. Ph.D. Thesis, Shanghai Jiao Tong University, Shanghai, China, 2019. (In Chinese).
17. Ma, W.; Zhang, K.; Du, Y.; Liu, X.; Shen, Y. Status of Sustainability Development of Deep-Sea Mining Activities. *J. Mar. Sci. Eng.* **2022**, *10*, 1508. [[CrossRef](#)]
18. Alhaddad, S.; Helmons, R. Sediment Erosion Generated by a Coandă-Effect-Based Polymetallic-Nodule Collector. *J. Mar. Sci. Eng.* **2023**, *11*, 349. [[CrossRef](#)]
19. Ziyu, Y.; Guocheng, Z.; Longfei, X.; Mingyue, L. Comparative Study on Collection Performance of Three Nodule Collection Methods in Seawater and Sediment-seawater Mixture. *Appl. Ocean. Res.* **2021**, *110*, 102606.
20. Zhang, Y.Y.; Dai, Y.; Zhu, X. Numerical Investigation of Recommended Operating Parameters Considering Movement of Polymetallic Nodule Particles during Hydraulic Lifting of Deep-Sea Mining Pipeline. *Sustainability* **2023**, *15*, 4248. [[CrossRef](#)]
21. Shih, T.-H.; Liou, W.W.; Shabbir, A.; Yang, Z.; Zhu, J. A new k- $\epsilon$  eddy viscosity model for high reynolds number turbulent flows. *Comput. Fluids* **1995**, *24*, 227–238. [[CrossRef](#)]
22. Chen, Y.; Xiong, H.; Cheng, H.; Chen, Y. Experimental study on the incipient motion of a single spherical particle in hydraulic collecting. *Zhongnan Daxue Xuebao (Ziran Kexue Ban) J. Cent. South Univ. (Sci. Technol.)* **2019**, *50*, 2831–2839. [[CrossRef](#)]
23. Zhao, G.; Xiao, L.; Lu, H.; Chen, Z. A case study of hydraulic collecting a single spherical particle. In Proceedings of the 27th International Ocean and Polar Engineering Conference, ISOPE 2017, San Francisco, CA, USA, 25–30 June 2017; pp. 30–38.
24. Zhao, G.C.; Xiao, L.F.; Zhao, W.J. Numerical and experimental study on vertical force of ball in suction flow field. In Proceedings of the 14th National Conference on Hydrodynamics and the 28th National Symposium on Hydrodynamics, Changchun, Jilin, China, 8 October 2017; pp. 476–482. (In Chinese).
25. Zhao, G.; Xiao, L.; Peng, T.; Zhang, M. Experimental Research on Hydraulic Collecting Spherical Particles in Deep Sea Mining. *Energies* **2018**, *11*, 1938. [[CrossRef](#)]
26. Sobota, J.; Boczarski, S.; Petryka, L.; Kotlinski, R.; Stoyanova, V. Slip Velocity in Nodules Vertical Flow—Experimental Results. In Proceedings of the Fourth (2001) Isope Ocean Mining Symposium, Szczecin, Poland, 23–27 September 2001; pp. 127–131.
27. Shen, Y.H. Minimum lifting velocity of solid—Liquid two—Phase flow in vertical pipe. *J. Univ. Sci. Technol. Beijing* **1999**, 519–522. (In Chinese) [[CrossRef](#)]
28. Yang, N.; Tang, H. Several considerations of the design of the hydraulic pick-up device. In Proceedings of the Fifth (2003) Isope Ocean Mining Symposium, Tsukuba, Japan, 15–19 September 2003; pp. 119–122.
29. Lee, M.; Cho, S.-g.; Choi, J.-S.; Kim, H.-W.; Hong, S.; Lee, T.H. Metamodel-Based Multidisciplinary Design Optimization of a Deep-Sea Manganese Nodules Test Miner. *J. Appl. Math.* **2012**, *2012*, 326954. [[CrossRef](#)]
30. Hu, Q.; Chen, J.; Deng, L.; Kang, Y.; Liu, S. CFD-DEM Simulation of Backflow Blockage of Deep-Sea Multistage Pump. *J. Mar. Sci. Eng.* **2021**, *9*, 987. [[CrossRef](#)]
31. Lim, S.J.; Kim, J.W.; Jung, S.T.; Cho, H.Y.; Lee, S.H. Deep Seawater flow Characteristics Around the Manganese Nodule Collecting Device. *Procedia Eng.* **2015**, *116*, 544–551. [[CrossRef](#)]
32. Jin, W.B.; Huang, X.P.; Gao, W.P. Experimental study on minimum Conveying speed of large particle material in vertical pipe. *Min. Res. Dev.* **1997**, 17–20. (In Chinese) [[CrossRef](#)]
33. Xiong, H.; Chen, Y.; Yang, N.; Xiao, J.; Li, L. Numerical study on settling and floating movements of a sphere particle flowing in a vertical pipe. In Proceedings of the 28th International Ocean and Polar Engineering Conference, Sapporo, Japan, 10–15 June 2018; pp. 176–182.
34. Pougatch, K.; Salcudean, M. Numerical modelling of deep sea air-lift. *Ocean. Eng.* **2008**, *35*, 1173–1182. [[CrossRef](#)]
35. Tauviqirrahman, M.; Jamari, J.; Susilowati, S.; Pujiastuti, C.; Setiyana, B.; Pasaribu, A.H.; Ammarullah, M.I. Performance Comparison of Newtonian and Non-Newtonian Fluid on a Heterogeneous Slip/No-Slip Journal Bearing System Based on CFD-FSI Method. *Fluids* **2022**, *7*, 225. [[CrossRef](#)]



36. Zhu, H.P.; Zhou, Z.Y.; Yang, R.Y.; Yu, A.B. Discrete particle simulation of particulate systems: Theoretical developments. *Chem. Eng. Sci.* **2007**, *62*, 3378–3396. [[CrossRef](#)]
37. Chen, Y.; Xiong, H.; Cheng, H.; Yu, C.; Xie, J. Effect of particle motion on the hydraulic collection of coarse spherical particles. *Acta Mech. Sin.* **2019**, *36*, 72–81. [[CrossRef](#)]
38. Wei, W.; Wang, Y.; Tao, T.; Chen, X.; Hu, N.; Ma, Y.; Yan, Q. A Study on Using Location-Information-Based Flow Field Reconstruction to Model the Characteristics of a Discharging Valve in a Hydrodynamic Retarder. *Machines* **2023**, *11*, 460. [[CrossRef](#)]
39. Ammarullah, M.I.; Hartono, R.; Supriyono, T.; Santoso, G.; Sugiharto, S.; Permana, M.S. Polycrystalline Diamond as a Potential Material for the Hard-on-Hard Bearing of Total Hip Prosthesis: Von Mises Stress Analysis. *Biomedicines* **2023**, *11*, 951. [[CrossRef](#)] [[PubMed](#)]
40. Jamari, J.; Ammarullah, M.I.; Santoso, G.; Sugiharto, S.; Supriyono, T.; Permana, M.S.; Winarni, T.I.; van der Heide, E. Adopted walking condition for computational simulation approach on bearing of hip joint prosthesis: Review over the past 30 years. *Heliyon* **2022**, *8*, e12050. [[CrossRef](#)] [[PubMed](#)]
41. CD-adapco. *User Guide, STAR-CCM+*; CD-adapco: Melville, NY, USA, 2016.
42. Salaha, Z.F.M.; Ammarullah, M.I.; Abdullah, N.N.A.A.; Aziz, A.U.A.; Gan, H.-S.; Abdullah, A.H.; Abdul Kadir, M.R.; Ramlee, M.H. Biomechanical Effects of the Porous Structure of Gyroid and Voronoi Hip Implants: A Finite Element Analysis Using an Experimentally Validated Model. *Materials* **2023**, *16*, 3298. [[CrossRef](#)]
43. Liu, L.; Gai, K.; Yang, J.; Guo, X. Numerical Investigation on the Dynamics of Mixture Transport in Flexible Risers during Deep-Sea Mining. *J. Mar. Sci. Eng.* **2022**, *10*, 1842. [[CrossRef](#)]
44. Zhao, G.C.; Xiao, L.F.; Hu, J.C.; Zhao, W.J. Experimental study on the mechanical characteristics of ellipsoidal coarse particles in the flow field of deep-sea hydraulic ore collection. *Shipbuilding of China* **2020**, *61*, 81–89.
45. Hong, S.; Hu, X. Research on Wear Characteristics and Experiment on Internal Through-Passage Components for a New Type of Deep-Sea Mining Pump. *Processes* **2021**, *10*, 58. [[CrossRef](#)]
46. Prakoso, A.T.; Basri, H.; Adanta, D.; Yani, I.; Ammarullah, M.I.; Akbar, I.; Ghazali, F.A.; Syahrom, A.; Kamarul, T. The Effect of Tortuosity on Permeability of Porous Scaffold. *Biomedicines* **2023**, *11*, 427. [[CrossRef](#)]
47. Putra, R.U.; Basri, H.; Prakoso, A.T.; Chandra, H.; Ammarullah, M.I.; Akbar, I.; Syahrom, A.; Kamarul, T. Level of Activity Changes Increases the Fatigue Life of the Porous Magnesium Scaffold, as Observed in Dynamic Immersion Tests, over Time. *Sustainability* **2023**, *15*, 823. [[CrossRef](#)]

**Disclaimer/Publisher’s Note:** The statements, opinions and data contained in all publications are solely those of the individual author(s) and contributor(s) and not of MDPI and/or the editor(s). MDPI and/or the editor(s) disclaim responsibility for any injury to people or property resulting from any ideas, methods, instructions or products referred to in the content.